Chapter 12

3D-Printed Artificial Organ Models for Surgical Applications

Chuchu Chen and Kaiyan Qiu

Abstract

Medical errors are one of the leading death causes in the United States, becoming a serious concern in clinical surgeries. Although full elimination of medical errors is unattainable, proper surgical planning and rehearsals on presurgical artificial organ models can reduce the error occurrences. However, current organ models miss multiple important features, such as a lack of tissue-mimicking properties and quantitative sensing feedback, significantly limiting their capabilities in advanced surgical planning and rehearsal. Therefore, the design and development of new methods and customized inks to fabricate patient-specific 3D-printed artificial organ models with accurate tissue-mimicking sensation and real-time operation feedback can be greatly beneficial to surgical applications and outcomes.

This chapter introduces relevant fabrication, properties, characterization, and applications of 3D-printed patient-specific prostate models with physical properties of tissue and integrated soft electronic sensors.

Key words 3D printing, Artificial organ models, Tissue-mimicking inks, Tactile sensors, Surgical applications

1 Introduction

Medical errors are a major concern in clinical practice. As early as centuries ago, clay and stone models were made into anatomical models to stimulate health conditions [1]. The study shows medical errors' rank as the third most significant cause of death in the United States after heart disease and cancer [2]. Although it is impossible to completely avoid errors in clinical procedures, surgical planning and rehearsal on more advanced and functional presurgical organ models are essential to lower the error rates in modern medical science [3, 4].

Conventional manufacturing techniques, such as milling or cutting methods or hand-made molds, show less accuracy and require more time and labor to build their structures [5, 6]. Additive manufacturing technology, also called 3D printing, was first introduced by Chuck Hull in 1983 [7]. To date, it has been recognized

as a revolution in the fields of manufacturing and fabrication and has evolved into one of the most feasible methods for creating complex organ models and other geometries [8].

Due to advantages of low manufacturing cost, easy availability, and customized options [9], layer-by-layer 3D printing has recently emerged as an alternative fabrication method for biomedical products, such as 3D-printed artificial organ models. 3D-printed patient-specific presurgical organ models have been utilized to aid in presurgical planning and surgical treatment analysis [10].

Currently, fused deposition modeling (FDM), material jetting (PolyJet), stereolithography (SLA), and inkjet 3D printing techniques have been used to fabricate organ models with commercial materials. The typical processes of 3D printing utilize the following steps. First, the original computed tomography (CT)/magnetic resonance imaging (MRI) for patient-specific organ models are identified and processed by specific software such as Vitrea and Mimics. This step will convert the data sets in the digital imaging and communications in medicine (DICOM) format into STereo-Lithography (STL) file [11, 12]. Second, in some cases, the initial STL file is rectified to removal of the imperfections by Computer-Aided Design (CAD) software packages to form refined STL file. Third, the refined STL file model is then imported into slicing software to generate G-code by horizontal layers. Finally, the G-code defines the printing pathway which is applied for the fabrication of 3D-printed organ models [4].

In view of their relatively low cost and high accuracy, rigid-plastic materials as filament for FDM printing or PolyJet technology are popular [13], and they have been used in the fields of cardiology [14], urology [15], neurology [16], and hepatology [17]. However, Young's moduli are much higher than the modulus values of most soft organ tissue samples, impeding the applications for surgical rehearsals [4, 18].

Elastomeric (rubber-like) materials possess excellent elasticity and flexibility because of the reconfiguration of long chains of the polymers and covalent cross-links, making the fabricated organ models have slightly better tactile sensation for surgical rehearsals than the models fabricated by rigid materials [19]. However, the discrepancy of the mechanical properties between these elastomeric materials and the related patient tissue is still large which inhibits surgical applications.

Organ models with powder-based materials can be fabricated through solidification with bindings by inkjet method. Although these models own less precise mechanical properties, they can still provide accurate geometry details, with low cost [20].

In addition, current 3D-printed organ models lack the capability for sensing operation pressure to give responses for more realistic surgical rehearsal. For example, Wake et al. [15] created anatomically accurate and patient-specific prostate and cancerous kidney models by FDM method. Their 3D-printed organ models
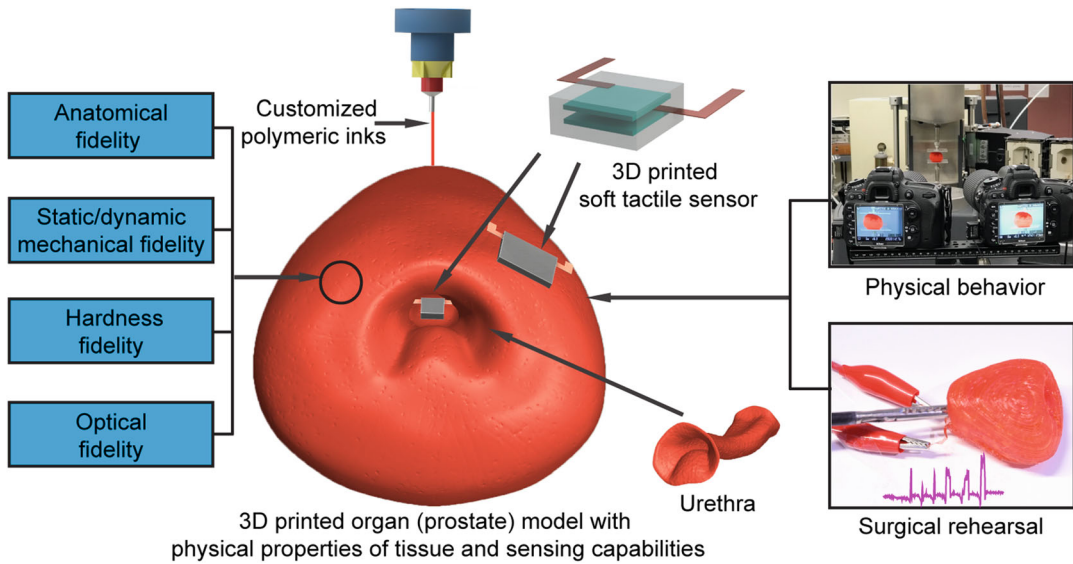
Fig. 1 Overview of the 3D-printed organ (prostate) model. (Source: Reproduced with permission from [4]. Copyright 2017, John Wiley & Sons)

can help surgeons to determine the position of tumor anatomy, assist them in finalizing surgical plans, and provide intraoperative guidance. However, these models lack function to provide quantitative feedback on the handling of surgical rehearsal which limits the accurate evaluation of operative handling before surgeries on patients.

To conclude, current 3D-printed organ models are important tools for routine surgical applications. However, to significantly remove the limitations for advanced surgical applications, there are still two major challenges waiting to be addressed: (1) how to accurately mimic the physical properties of organ tissue and (2) how to provide quantitative feedback resulting from organ and tissue handling [21].

Here, we describe, in detail, how to develop 3D-printed patient-specific prostate models using customized polymeric inks for surgical planning and rehearsal (Fig. 1). The physical properties of the 3D-printed prostate model are closely matching those of prostate tissue which can enable the models for applications in suturing and tool handling. The integrated tactile sensors can provide quantitative feedback for multiple surgical operations.

2   Materials

2.1   Customized Polymeric Inks

1. Silicone sealant (Loctite SI 595™ CL).
2. Silicone grease (#LP20, Trident®).
3. Procyinyl Red GS (ICI America Inc.).

4. Fumed silica (Powder 7 nm).

5. Dichloromethane.

6. Pluronic® F3 127.

7. Lithium chloride.

8. Acrylamide monomer.

9. Polyacrylamide (Mw 5,000,000–6,000,000).

10. Milli-Q ultrapure water.

11. Ethylene glycol.

12. N,N′-methylenebisacrylamide crosslinking agent.

13. Irgacure 1173 photoinitiator Badische Anilin- und Sodafabrik (BASF).

14. Silicone-based dielectric elastomer (Loctite 5039 Nuva-Sil, Henkel).

15. Semicosil 912 (Wacker).

16. Elastosil CAT UV catalyst (Wacker).

17. Copper tape.

18. Benzophenone.

19. Acetone.

2.2 Equipment

1. Plenary centrifugal mixer (ARE-310, Thinky).

2. Custom-built 3D printing system (AGS 100, Aerotech).

3. High-precision digital dispensers (Ultimus V, EFD).

4. Surgical punch biopsy instrument with a circular hollow blade (8 mm diameter).

5. Mechanical analyzer (RSA-G2, TA Instruments).

6. Nanoindentation system (Nanoindenter XP, MTS).

7. Fiber optic equipment (Ocean Optics).

8. Magnetic bearing rheometer (AR-G2, TA Instruments).

9. Magnetic resonance imaging (MRI) system (9.4 Tesla).

10. ANSYS Workbench 17.1.

11. Two Nikon cameras (D750) with lenses (Nikon AF Micro NIKKOR 200 mm f/4D) and tripod.

12. Nikon ML-L3.

13. 3D scanning (HDI 109, GoMeasure3D).

14. Soft capacitive sensor device.

15. UV system (Omnicure S1500, Excelitas Technologies).

16. Endoscope (Gyrus ACMI) and endoscopic tower station (Stryker).

17. Nanopositioning stage (ANT130-LZS, Aerotech).

18. Digital scale with a flat surface.

19. LED light source (L9000, Stryker).

20. Endoscopic camera (1288 HD 3-Chip, Stryker).

21. HD information management system (SDC Ultra, Stryker).

22. High flow insufflator (40 L, Stryker).

23. High-Definition Television (HDTV) surgical display (WiSeTM, Stryker).

24. Surgical needle.

25. Surgical thread (ETHICON 3-0 PERMA-HAND SILK).

26. Surgical grasper.

27. Surgical scissors.

2.3   Software

1. Vitrea® software (Canon Medical).

2. Slic3r open-source software.

3. Mimics software package (Materialise NV).

4. CloudCompare open-source software.

5. MeshLab software.

6. SolidWorks software (Dassault Systèmes).

3   Methods

3.1   Fabrication of Customized Polymeric Inks

1. Set silicone sealant as active agent for vulcanization, silicone grease as bulking agent, Procyinyl Red GS as coloring agent, and fumed silica as a thickening agent, respectively (Fig. 2a).

2. Mix active agent and the bulking agent at proper weight ratios (weight ratio of active agent to bulking agent for inks 1, 2, and 3 are ca. 0.95:3.05, 0.90:3.10, and 0.82:3.18) to achieve different values of Young's modulus via plenary centrifugal mixer at 2000 rpm for 10 min to form the primary component of the customized polymeric inks (Fig. 2b; *see* **Notes 1** and **2**).

3. Mix customized polymeric inks (10 g) with 1% (w/v) coloring agent dichloromethane (DCM) solution (0.5 mL) at 20:1 (w/v) ratio via the mixer at 2000 rpm for 10 min.

4. Remove excessive DCM solvent from the customized polymeric inks via vacuum before use.

5. Add the trivial amount of thickening agent to adjust the viscosity of the precursor for proper printability if necessary.

3.2   3D Printing of Organ Models

1. Edit the MR image pack (1 mm resolution) of the patient prostate organ via Vitrea® software to form a patient organ (prostate) STL model.
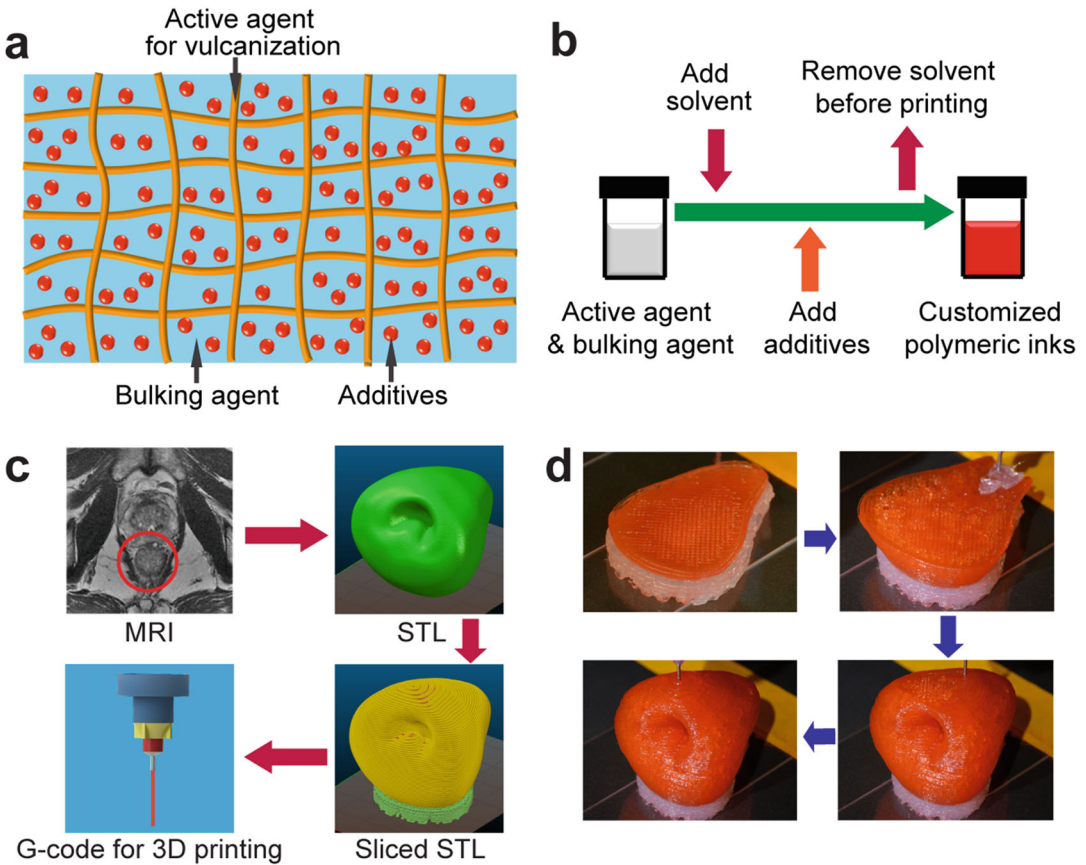
Fig. 2 3D printing of the prostate model. (**a**) Schematic of the composite components of the customized polymeric inks. (**b**) Preparation procedure for the customized polymeric inks. (**c**) Procedure for converting patient-specific MRI to G-code for the 3D printing process. (**d**) 3D printing process of the prostate model using the customized polymeric ink. (Source: Reproduced with permission from [4]. Copyright 2017, John Wiley & Sons)

2. Slice the STL model by Slic3r open-source software and generate G-code for printing (Fig. 2c).

3. 3D print the models via G-code using a custom-built 3D printing system with two independent z-axis heads (*see* **Notes 2**, **3**, **4**, and **5**).

4. Deposit the customized polymeric ink and supporting ink from two dispensing apparatuses controlled by two high-precision dispensers through nozzles with 610 μm inner diameters (20 GA GP.023X.25) and 500 μm layer heights for printing. The nozzle sizes can be varied based on the fabrication requirements for different organ models (Fig. 2d).

5. Remove the supporting ink mechanically after the inks in the model were fully cured at ambient temperature in air.

6. Use 33–40 wt% Pluronic® F127 in water as the supporting ink for more complex organ models, and the supporting ink can be later removed via flushing with water at 4 °C (*see* **Note 2**).

3.3 Characterization of Prostate Tissue and Customized Polymeric Inks

1. Use radical prostatectomy to collect human prostate.

2. Cut prostate tissue into approximately 8 mm × 5 mm (D × H) cylindrical samples with flat surfaces via a surgical punch biopsy instrument with a circular hollow blade (8 mm diameter) for static/dynamic compression and hardness tests.

3. 3D print customized polymeric inks into cylindrical samples with similar dimensions as the tissue samples for direct comparison of results.

4. Place tissue samples on the paten.

5. Carry out static compression tests for both prostate tissue samples and 3D-printed cylindrical samples for up to 0.20 strain at a rate of 0.1 s^{-1} (0.5 mm/s) and dynamic compression tests at frequencies of 0.1–20 Hz and at strains of 0.05, 0.10, and 0.20 by RSA-G2 mechanical analyzer.

6. Conduct hardness tests for both prostate tissue samples and 3D-printed cylindrical samples on a nanoindentation system at a strain rate of 0.5 s^{-1} for both loading and unloading with a depth limit of 20 μm.

7. Evaluate the optical reflection of the gross tissue and colored 3D-printed samples with fiber optic equipment.

3.4 Rheological Characterization

1. Characterize the rheology properties of the customized polymeric inks and its corresponding active and bulking agents on a magnetic-bearing rheometer with a steel plate (25 mm diameter) in Smart Swap geometry at 25 °C.

2. Conduct flow experiments via a logarithmic sweep of shear rate at 0.1–1000/s with a 500 μm gap between the Smart Swap geometry and the lower geometry.

3.5 MRI of 3D-Printed Prostate Model

1. Put the 3D-printed prostate model in a 31 cm bore in an MRI System (9.4 Tesla).

2. Define the field of view to 5 mm × 5 mm × 5 mm.

3. Set the number of scans and views to 200 and 128,000, respectively.

4. Carry out the MR imaging of the 3D-printed prostate model by the MRI system.

3.6 3D Registration for Anatomical Fidelity

1. Obtain the 3D model of the printed prostate from the MRI image stack using the Mimics software package.

2. Realize the 3D registration of the STL files between the 3D-printed prostate model and the patient prostate model by CloudCompare software.

3. Use CloudCompare to obtain a distance heatmap and a histogram of the distances of the corresponding points on the surface for the overlaid 3D models, using a comparison of 3×10^5 voxels on the surface in 40 iterations.

4. Calibrate the arbitrary distance scale generated by CloudCompare to millimeter scale.

5. Determine the print fidelity by the percentile of points that fell between a given error margin from the histogram of distances.

3.7 Finite Element Method (FEM) Simulation

1. Employ the FEM software (ANSYS Workbench 17.1) for simulation with static structural component.

2. Use an Ogden hyperelastic third model [22] to fit the measured strain-stress data and generate curve.

3. Define the contacts between the FEM model and plates as frictional with a friction coefficient of 10.

4. Generate 137,905 nodes for the model with a size of 45.14 mm × 41.70 mm × 30.95 mm (L × W × H).

5. Set the element size of the prostate model as 3 mm and the surface size of the contacting areas with the top and bottom plates to be 1 mm.

6. Sweep in the Z-axis with one division to mesh the top and bottom plates and divide the edges into 20 segments (each with a bias factor of 5).

7. Determine the element types via ANSYS Workbench 17.1.

8. Assign about 4.64 mm displacement from the original position in the Z-axis to the top plate and fix the bottom plate to compress the prostate model by approximately 15.0% of its height.

9. Apply 9.28 s as the total compression time to make the simulation speed consistent with the actual testing one.

10. Extract the total 3D displacement of the feature dots.

11. Record the reaction force (up to 1.74 N at 15%) of the whole compression in the Z-direction.

3.8 3D Displacement Measurement Using Stereo System with Feature Dots During Model Compression

1. Design a stereo-system-based 3D displacement measurement procedure. First, mount two Nikon cameras (D750) with lenses (Nikon AF Micro NIKKOR 200 mm f/4D) on a single tripod. Then, place the camera-tripod system in front of the mechanical analyzer at about 1 m distance. Adjust the foci of the lenses and set camera parameters to minimize timing differences. Use Nikon ML-L3 as a remote controller to wirelessly control the two cameras. Finally, use the shutter button on the

controller to trigger the continuous shooting of the two cameras and reduce the image blur.

2. Apply the procedure to track the 3D trajectories of the feature dots on the 3D-printed prostate model (ink 2, 100% fill density) during model compression by a RSA-G2 mechanical analyzer. Conduct static compression tests for up to 0.20 strain at a rate of 0.1 s^{-1} (0.5 mm/s) and dynamic tests at frequencies of 0.1–20 Hz and at strains of 0.05, 0.10, and 0.20.

3. Read the reaction force during the compression test from the mechanical analyzer.

3.9 Mapping of the Feature Dots to the Corresponding Locations on the FEM Simulation Model

1. Coat a thin layer of baby powder on a 3D-printed prostate model with feature dots for 3D scanning.

2. Import the scanned model and the FEM simulation model into the CloudCompare software for 3D registration with a uniform coordinate system.

3. Use the location coordinates (x, y, z) of the feature dots on the scanned model to map the corresponding locations with the same coordinates on the FEM simulation model.

3.10 Design, 3D Printing, and Calibration of Soft Tactile Sensor

1. Design the capacitive tactile sensor which consists of a polyacrylamide-based ionic hydrogel as electrodes and a silicone-based dielectric elastomer as an electroactive component (*see* **Note 2**).

2. Prepare the ionic hydrogel with 21.48 wt% lithium chloride, 7.90 wt% acrylamide monomer, 3.16 wt% polyacrylamide, 29.64 wt% Milli-Q ultrapure water, 37.60 wt% ethylene glycol, 0.13 wt% N,N′-methylenebisacrylamide crosslinking agent, and 0.08 wt% Irgacure 1173 photoinitiator.

3. Mix Loctite 5039 Nuva-sil and Semicosil 912 at a ratio of 3:2, and addition of Elastosil CAT UV catalyst at a ratio of 1:10 with respect to the Semicosil 912 base as the silicone elastomer.

4. Print a soft capacitive sensor device by alternately depositing layers of two different materials (polyacrylamide-based ionic hydrogel and silicone-based dielectric elastomer).

5. Expose the printed sensor to a UV system for photopolymerization.

6. Calibrate the soft sensor by applying varying pressures to the device and measuring the changes in capacitance. Mount a metal bar on the vertical axis of a nanopositioning stage to apply cycles of press release to the device by different the vertical position of the bar to obtain corresponding values. Record the applied force with a digital scale with a flat surface. Use the sensor placed on the digital scale to observe the capacitance changes (*see* **Note 2**).
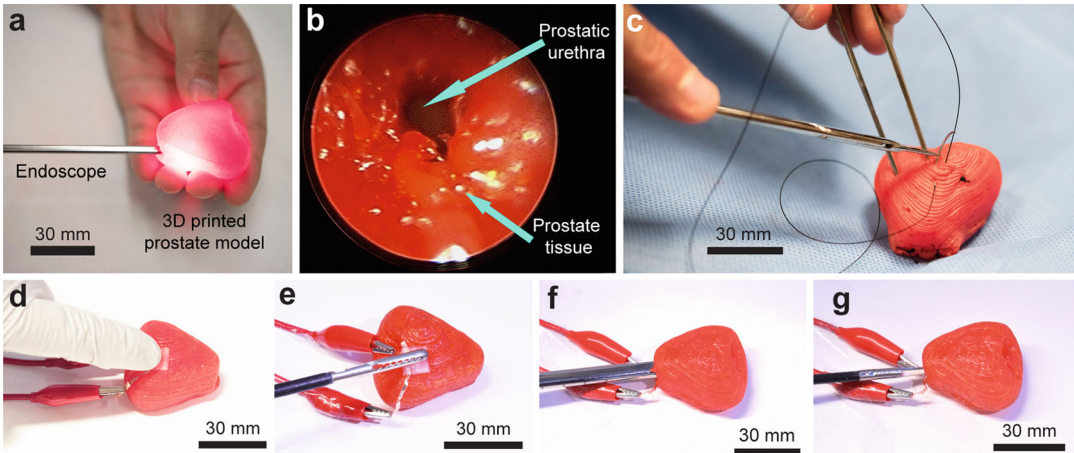
Fig. 3 Quantitative surgical rehearsal using the 3D-printed prostate model. (**a**) Surgical rehearsal involves applying an endoscope in the urethra of the 3D-printed prostate model. (**b**) Endoscopic view of the urethra inside of the 3D-printed prostate model. (**c**) Surgical suturing on the 3D-printed prostate model. (**d**, **e**) Quantitative surgical rehearsal involving the 3D-printed prostate model upon applying a finger (**d**) and a surgical grasper (**e**) on a sensor integrated into the model's outer surface, respectively. (**f**, **g**) Quantitative surgical rehearsal involving the 3D-printed prostate model when applying an endoscope (**f**) and surgical scissors on a sensor integrated into the model's urethra surface (**g**). (Source: Reproduced with permission from [4]. Copyright 2017, John Wiley & Sons)

3.11 Advanced Surgical Rehearsal Using the 3D-Printed Prostate Model

1. Assemble an endoscope, an LED light source, an endoscopic, an HD information management system, a high flow insufflator, and an HDTV surgical into an endoscope system (Fig. 3a).

2. Insert an endoscope from the system into the urethra of the model to observe the endoscopic view from the surgical display in the endoscopic tower station (Fig. 3b; *see* **Notes 2** and **6**).

3. Place the printed prostate model between kidney and bladder models and carry out presurgical rehearsal under kidney–urethra–bladder background (*see* **Notes 2** and **6**).

4. Conduct surgical suturing on the surface of the 3D-printed prostate model with the assistance of a surgeon and by utilizing a surgical needle for penetration and surgical thread for suturing (Fig. 3c; *see* **Notes 2** and **6**).

5. Put finger (Fig. 3d), surgical grasper (Fig. 3e), endoscope (Fig. 3f), and surgical scissors (Fig. 3g) on the sensors integrated on the surface and interior of the 3D-printed prostate model (*see* **Note 2**).

6. Apply three quick press–release and three press–hold–release cycles for each application (*see* **Note 2**).

7. Convert signal responses of capacitance changes of the 3D-printed sensor into values of applied pressures via sensor calibration data (*see* **Note 2**).

4 Notes

1. In our work on 3D-printed prostate models, we successfully developed the physical properties of tissue and pressure-sensing feedback within the organ models for advanced surgical applications. However, many other efforts can be applied to provide additional functions and capabilities of the models.

2. In another related and follow-up work, we further demonstrated the application of 3D printing for patient-specific aortic root models with internally integrated sensor array using multiple customized inks with a variety of properties for different model components (in the prostate model, only one customized ink was applied). The models were used as a preplanning platform for minimally invasive procedures, such as transcatheter aortic valve replacement (TAVR) [23]. The 3D-printed aortic root models were used for clinic result comparison, hemodynamic studies, and paravalvular leak identification. The internally integrated tactile sensor array (nine sensing pixels) with area pressure feedback (in the prostate model, the sensor was externally integrated on surface of the model with only one sensing pixel) was applied as a tool for evaluation and identification of the suitable device sizes and implantation locations. These models are potential candidates for next-generation medical devices to mitigate the risks of postoperative complications.

3. Tissue-mimicking inks with better tissue fidelity for mechanical properties in high strain range need to be further developed. The goal is to tailor the inks to meet the requirements in certain conditions, such as mimicking of the pulsation of cardiac muscle in the presurgical organ models.

4. Anisotropic properties in real organ tissue need to be realized in the presurgical organ models through 3D printing process by controlling the orientation of printing pathways [24, 25] and imbedding fillers [26, 27].

5. Most of the 3D-printed organ models reported so far, including our prostate models and aortic root models, are static models without dynamic functions. In the future, pulsation function through proper actuation needs to be integrated with 3D-printed organ models (such as cardiac models), to provide more realistic surgical practice and feedback.

6. The integration of virtual and assisted reality tools into the 3D-printed organ models needs to be developed to visualize finer features through complex surgical simulation.

Acknowledgments

References

1. Owen H (2012) Early use of simulation in medical education. Simul Healthc 7(2): 102–116

2. Makary MA, Daniel M (2016) Medical error—the third leading cause of death in the US. BMJ 353:i2139

3. Qiu K, Haghiashtiani G, McAlpine MC (2018) 3D printed organ models for surgical applications. Annu Rev Anal Chem (Palo Alto, Calif) 11(1):287

4. Qiu K, Zhao Z, Haghiashtiani G, Guo SZ, He M, Su R et al (2018) 3D printed organ models with physical properties of tissue and integrated sensors. Adv Mater Technol 3(3): 1700235

5. Jin Z, Li Y, Yu K, Liu L, Fu J, Yao X et al (2021) 3D printing of physical organ models: recent developments and challenges. Adv Sci 8(17):2101394

6. Klein H, Schneider W, Alzen G, Voy E, Günther R (1992) Pediatric craniofacial surgery: comparison of milling and stereolithography for 3D model manufacturing. Pediatr Radiol 22(6):458–460

7. Whitaker M (2014) The history of 3D printing in healthcare. Bull R Coll Surg Engl 96(7): 228–229

8. Budhiraja S, Ashok PP, Mathiyazhagan K (2021) Challenges and materials in artificial organ manufacturing. In: Advances in engineering materials. Springer, pp 637–653

9. Dhinesh S, Kumar KS (2020) A review on 3D printed sensors. IOP Conf Ser Mater Sci Eng (IOP Publishing) 764(1):012055

10. Yan Q, Dong H, Su J, Han J, Song B, Wei Q et al (2018) A review of 3D printing technology for medical applications. Engineering 4(5):729–742

11. Mitsouras D, Liacouras P, Imanzadeh A, Giannopoulos A, Cai T, Kumamaru K (2015) Medical 3D printing for the radiologist. RadioGraphics Press

12. Giannopoulos AA, Mitsouras D, Yoo S-J, Liu PP, Chatzizisis YS, Rybicki FJ (2016) Applications of 3D printing in cardiovascular diseases. Nat Rev Cardiol 13(12):701–718

13. Vukicevic M, Mosadegh B, Min JK, Little SH (2017) Cardiac 3D printing and its future directions. JACC Cardiovasc Imaging 10(2): 171–184

14. Farooqi KM, Lengua CG, Weinberg AD, Nielsen JC, Sanz J (2016) Blood pool segmentation results in superior virtual cardiac models than myocardial segmentation for 3D printing. Pediatr Cardiol 37(6):1028–1036

15. Wake N, Chandarana H, Huang W, Taneja S, Rosenkrantz A (2016) Application of anatomically accurate, patient-specific 3D printed models from MRI data in urological oncology. Clin Radiol 71(6):610–614

16. Anderson JR, Thompson WL, Alkattan AK, Diaz O, Klucznik R, Zhang YJ et al (2016) Three-dimensional printing of anatomically accurate, patient specific intracranial aneurysm models. J Neurointerv Surg 8(5):517–520

17. Zein NN, Hanouneh IA, Bishop PD, Samaan M, Eghtesad B, Quintini C et al (2013) Three-dimensional print of a liver for preoperative planning in living donor liver transplantation. Liver Transpl 19(12): 1304–1310

18. Wurm G, Tomancok B, Pogady P, Holl K, Trenkler J (2004) Cerebrovascular stereolithographic biomodeling for aneurysm surgery. J Neurosurg 100(1):139–145

19. Loadman M (1999) Analysis of rubber and rubber-like polymers. Springer

20. Oishi M, Fukuda M, Yajima N, Yoshida K, Takahashi M, Hiraishi T et al (2013) Interactive presurgical simulation applying advanced 3D imaging and modeling techniques for skull base and deep tumors. J Neurosurg 119(1):94–105

21. Gómez-Ciriza G, Hussain T, Gómez-Cía T, Valverde I (2015) Potential of 3D-printed models in planning structural interventional procedures. Interv Cardiol 7(4):1–8

22. Ogden RW (1972) Large deformation isotropic elasticity–on the correlation of theory and experiment for incompressible rubberlike solids. Proc R Soc Lond A Math Phys Sci 326(1567):565–584

23. Haghiashtiani G, Qiu K, Zhingre Sanchez JD, Fuenning ZJ, Nair P, Ahlberg SE et al (2020) 3D printed patient-specific aortic root models with internal sensors for minimally invasive applications. Sci Adv 6(35):eabb4641

24. Johnson BN, Lancaster KZ, Zhen G, He J, Gupta MK, Kong YL et al (2015) 3D printed anatomical nerve regeneration pathways. Adv Funct Mater 25(39):6205–6217

25. Zou R, Xia Y, Liu S, Hu P, Hou W, Hu Q et al (2016) Isotropic and anisotropic elasticity and yielding of 3D printed material. Compos Part B 99:506–513

26. Gnanasekaran K, Heijmans T, Van Bennekom S, Woldhuis H, Wijnia S, De With G et al (2017) 3D printing of CNT-and graphene-based conductive polymer nanocomposites by fused deposition modeling. Appl Mater Today 9:21–28

27. Valentine AD, Busbee TA, Boley JW, Raney JR, Chortos A, Kotikian A et al (2017) Hybrid 3D printing of soft electronics. Adv Mater 29(40): 1703817